Direct Observation of Magnetic Domain and Magnetization Reversal on Prussian Blue-Based Magnetic Films

Shuntaro Nagashima,[†] Yuji Yahagi,[†] Masamichi Nishino,[‡,§] Takehiro Yamaoka,[∥] Kosuke Nakagawa,[#] Junhao Wang,[†] Shin-ichi Ohkoshi,[#,*] and Hiroko Tokoro[†,#,*]

[†]Department of Materials Science, Faculty of Pure and Applied Sciences, University of Tsukuba, 1-1-1 Tennodai, Tsukuba, Ibaraki 305-8573, Japan

[‡]Research Center for Advanced Measurement and Characterization, National Institute for Materials Science, 1-2-1 Sengen, Tsukuba, Ibaraki 305-0047, Japan

[§]Research Center for Materials Nanoarchitectonics, National Institute for Materials Science, 1-1 Namiki, Tsukuba, Ibaraki 305-0044, Japan

[∥]Analysis Systems Solution Development Department, Metrology and Analysis Systems Product Division, Hitachi High-Tech Co. 3-2-1 Sakado, Takatsu-ku, Kawasaki, Kanagawa 213-0012, Japan

[#]Department of Chemistry, School of Science, The University of Tokyo, 7-3-1 Hongo, Bunkyo-ku, Tokyo 113-0033, Japan

ABSTRACT: Knowledge of the magnetic domain is indispensable for understanding the magnetostatic properties of magnets. However, up to date, magnetic domain has not yet reported in the field of molecule-based magnets. Herein, we study the magnetic domains of molecule-based magnets. Two magnetic films of iron/chromium hexacyanidochromate $Fe_xCr_{1-x}[Cr(CN)_6]_{2/3}\cdot 5H_2O$ (x= 0; **Film 1** and x= 0.2; **Film 2**) were prepared for investigation. The temperature evolution of surface magnetization was measured using magnetic force microscopy. **Film 1** showed a magnetic domain below Curie temperature (T_C) and its positive-magnetic polarization increased monotonously with decreasing temperature, while **Film 2** showed positive magnetic polarization below T_C and switches from positive to negative magnetization through a demagnetization state at 146 K. This study originally reports the temperature variation of magnetization state at the magnetization reversal. The magnetic domains appeared as a maze pattern with an approximate domain size of one-to-several micrometers. This work shows that the research on molecule-based magnets can be expanded from magnetochemistry to the magnetostatic engineering of bulk magnets, molecule-based magnetostatic engineering.

INTRODUCTION

Typical magnetic materials such as metal–alloy magnets, rare earth magnets, and ferrite magnets are widely used in daily life and their magnetic mechanisms have been extensively studied. Forty years ago, researchers discovered bulk magnets composed of metal ions and organic molecules. These magnets were named molecule-based magnets or molecular magnets.[1] Since then, many molecule-based magnets have been developed in the chemistry field.[2–20] The orbital and spin angular momenta of each magnetic atom in a molecule-based magnet can be predicted from the ligand fields of the coordinated ligands and/or organic radicals. The magnetic interactions between the magnetic atoms (such as superexchange interactions, double-exchange interactions, and magnetic dipole–dipole interactions) can also be deduced, although in most cases, only the magnetic interactions between the nearest neighboring magnetic atoms contribute to the magnetic properties.[21–24] Moreover, one can design one-, two-, or three-dimensional structures of the spin network and the chiral structure of molecule-based magnets. Therefore, one can design the magnetic properties [saturation magnetization (M_s), Curie temperature (T_C), and coercive field (H_c)] by selecting the metal ions, radicals, and coordinated ligands considering the magnetic dimensionality of the spin network and the superexchange interactions between magnetic sites. The above investigations have led to new magneto-functionalities and developments such as photo-sensitive magnetism, pressure-responsive magnetism, superionic-conduction magnetism, gas-responsive magnetism, and transparent colored magnetic thin films.[25–48] Therefore, molecule-based magnets are expected as a proof-of-concept for advanced magnetic functions and applications (e.g., advanced magnetic sensors and external-stimuli-induced magnetic recordings), which have not been realized to date. However, magnetic domains in molecule-based magnets have not been studied. As information on magnetic domains is essential for upscaling a research-level of magnetic material to a practically usable magnetic material, observing the magnetic domain and evaluating the performance of a molecule-based magnet as a conventional magnet (e.g., evaluating its magnetic surface properties) are important tasks (Supporting Information §1). Although single-domain and vortex-magnetic states have been reported in nanoparticles of Prussian blue analogs,[33,36] there have been no reports on magnetic domains in three-dimensional ferromagnetic materials with a ferromagnetic multidomain structure (Figures 1 and S1). The present work reveals the magnetic domains in two molecule-based magnets. The target samples are two Prussian blue analogs: iron/chromium hexacyanidochromate $Fe_xCr_{1-x}[Cr(CN)_6]_{2/3}\cdot 5H_2O$ films with x = 0 (**Film 1**) and x = 0.2 (**Film 2**). **Film 1** showed a magnetic domain below Curie temperature (T_C) and its positive-magnetic

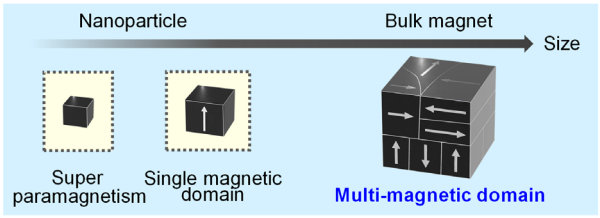

Figure 1. Illustration of the size dependence of the magnetization state. Nanoparticles with extremely small sizes indicate superparamagnetism, while larger nanoparticles exhibit a single magnetic domain. Bulk magnets exhibit multiple magnetic domains. Observations of single magnetic domains and vortex-magnetic states in nanoparticles of Prussian blue analogs were reported in previous studies.[33, 36] In this study, the focus was on Prussian blue–based magnets that exhibit multiple magnetic domains.

polarization increased monotonously with decreasing temperature, while **Film 2** showed positive magnetic polarization below T_C and switches from positive to negative magnetization through a demagnetization state at 146 K. Monte Carlo calculations presented the theoretical insight of magnetization reversal where positive magnetization is once demagnetized, and negative magnetization develops from the demagnetized state.

RESULTS AND DISCUSSION

Electrochemically Synthesized Films and their Morphology and Crystal Structures

Magnetic $Fe_xCr_{1-x}[Cr(CN)_6]_{2/3}\cdot 5H_2O$ films were prepared as described in the previous literature (Figure 2a).[48] The Fe^{3+} and Cr^{3+} ions in aqueous mixed solutions of $K_3[Cr(CN)_6]$ (0.5 mmol dm^{-3}), $CrCl_3$ (7.5 mmol dm^{-3} for $x = 0$ and 1.4 mmol dm^{-3} for $x = 0.2$), and $FeCl_3$ (6.1 mmol dm^{-3} for $x = 0.2$) were electrochemically reduced to Fe^{2+} and Cr^{2+}, respectively. In the reduced mixed solution, Fe^{2+} and Cr^{2+} were reacted with $[Cr^{III}(CN)_6]^{3-}$ to form the product $Fe^{II}_xCr^{II}_{1-x}[Cr^{III}(CN)_6]_{2/3}\cdot 5H_2O$. At constant reduction potential (−840 mV vs. Saturated Calomel Electrode (SCE)) and a loaded electrical capacity of 0.6 C, thin films of insoluble polynuclear metal cyanides were deposited on an electrode surface (SnO_2-coated glass). Elemental analyses of the prepared samples yielded a formula of $Cr^{II}[Cr^{III}(CN)_6]_{2/3}\cdot 5H_2O$ (**CrCr**) in **Film 1** and $Fe_{0.20}Cr_{0.80}[Cr(CN)_6]_{2/3}\cdot 5.3H_2O$ (**FeCrCr**) in **Film 2.**

Film 1 appeared as a transparent thin film on the SnO_2-coated glass (Figure 2b). From scanning electron microscopy (SEM) images, the thickness of the prepared film was determined as 1.70 ± 0.06 μm. Atomic force microscopy (AFM) images revealed a smooth and homogenous film surface with an uneven width of 0.58 ± 0.22 μm (Figures 2b and S2a). The mid-IR spectrum of **Film 1** shows a peak at 2190 cm^{-1} attributable to the CN stretching frequency of Cr^{II}–NC–Cr^{III} (Figure S3a).[48] The powder X-ray diffraction (PXRD) pattern of powder-form **CrCr** at 300 K revealed a cubic crystal structure (space group: $Fm\bar{3}m$) with a lattice constant of 10.4124(5) Å (Figure S4a and Table S1). The crystallite size estimated by Rietveld analysis was ca. 56 nm. The XRD pattern of the film sample (Figure S4b) is similar to that of the powder sample, even though the ratios of peak intensities at 24.2°, 34.4°, and 38.6° differ slightly from that of the powder sample. This difference in peak intensities indicates that the (220) plane is oriented slightly perpendicular to the substrate plane (Figure S5). **Film 2** appeared as a purple thin film on the SnO_2-coated glass (Figure 2c). SEM images of this film revealed a thickness of 1.76 ± 0.05 μm. AFM images confirmed a smooth and homogeneous thin film with an uneven width of 0.45 ± 0.14 μm (Figures 2c and S2b). Energy Dispersive X-ray Spectroscopy analysis of the SEM and transmission electron microscopy (TEM) images confirmed the homogenous distributions of iron, chromium, carbon, nitrogen, and oxygen elements in the film sample (Figures S6 and S7). The mid-IR spectrum of **Film 2** shows a peak at 2181 cm^{-1} attributable to the CN stretching frequencies of mixed Fe^{II}–NC–Cr^{III} and Cr^{II}–NC–Cr^{III} (Figure S3b).[48] The ultraviolet–visible (UV–vis) spectrum (Figure S8) shows a large broad absorption band with the maximum intensity at 508 nm, originating from intervalence transfer between Fe^{II} and Cr^{III}. The PXRD pattern of powder-form **FeCrCr** at 300 K revealed a cubic crystal structure (space group: $Fm\bar{3}m$) with a lattice constant of 10.4411(5) Å (Figure S9a and Table S2). The crystallite size estimated by Rietveld analysis was ca. 60 nm. The XRD pattern of the film sample (Figure S9b) is similar to that of the powder sample, even though the ratios of peak intensities at 24.1°, 34.4°, and 38.6° indicate that the (220) plane is oriented perpendicular to the substrate plane (Figure S10).

Magnetic Properties Determined from Superconducting Quantum Interference Device (SQUID) Measurements

The magnetic properties of **Film 1** were measured using a SQUID. In the magnetization versus temperature curves of this film, spontaneous magnetization appears below T_C (244 K; see Figure 2d). From the magnetization versus external magnetic field (H_{ex}) plots obtained under in-plane and out-of-plane H_{ex}, the H_c values at 153 K were determined as 40 and 70 Oe, respectively (Figure S11a). These observed magnetizations reproduce the literature-reported magnetic properties, which are explained by ferrimagnetism induced by antiferromagnetic coupling between the magnetic spins of Cr^{II} (S= 2) and Cr^{III} (S= 3/2) (upper part of Figure 2d).[48]

The magnetic properties of **Film 2** are shown in Figure 2e. The magnetization of this film was slightly positive below T_C (222 K) but negative below the compensation temperature T_{comp} (134 K). These temperature-dependent magnetizations manifest from mixed ferro-ferrimagnetism[23,24,48] involving two types of exchange couplings: a ferromagnetic interaction between Fe^{II} (S= 2) and Cr^{III} (S= 3/2) and an antiferromagnetic interaction between Cr^{II} (S= 2) and Cr^{III} (upper part of Figure 2e). The magnetization reversal at T_{comp} is the result of summing the temperature dependences of the positive magnetization due to the Cr^{II} sublattice and the negative magnetizations due to the Fe^{II} and Cr^{III} sublattices. The H_c values at 175, 134, and 113 K were 870, 2410, and 2890 Oe, respectively, under the in-plane H_{ex} and 1280, 1590, and 1450 Oe, respectively, under the out-of-plane H_{ex} (Figure S11b).

Surface Magnetism and Magnetic Domain Observed using MFM Measurements

The surface-magnetized states and magnetic domains were observed by the MFM measurements. The magnetic moment is detected as a phase-difference in the cantilever oscillations. The magnitude and direction of the phase-difference indicate the strength and direction (positive or negative) of the magnetic moment on the film surface, respectively (Figure S12). Figure 3a plots the detected frequency versus phase-difference on **Film**

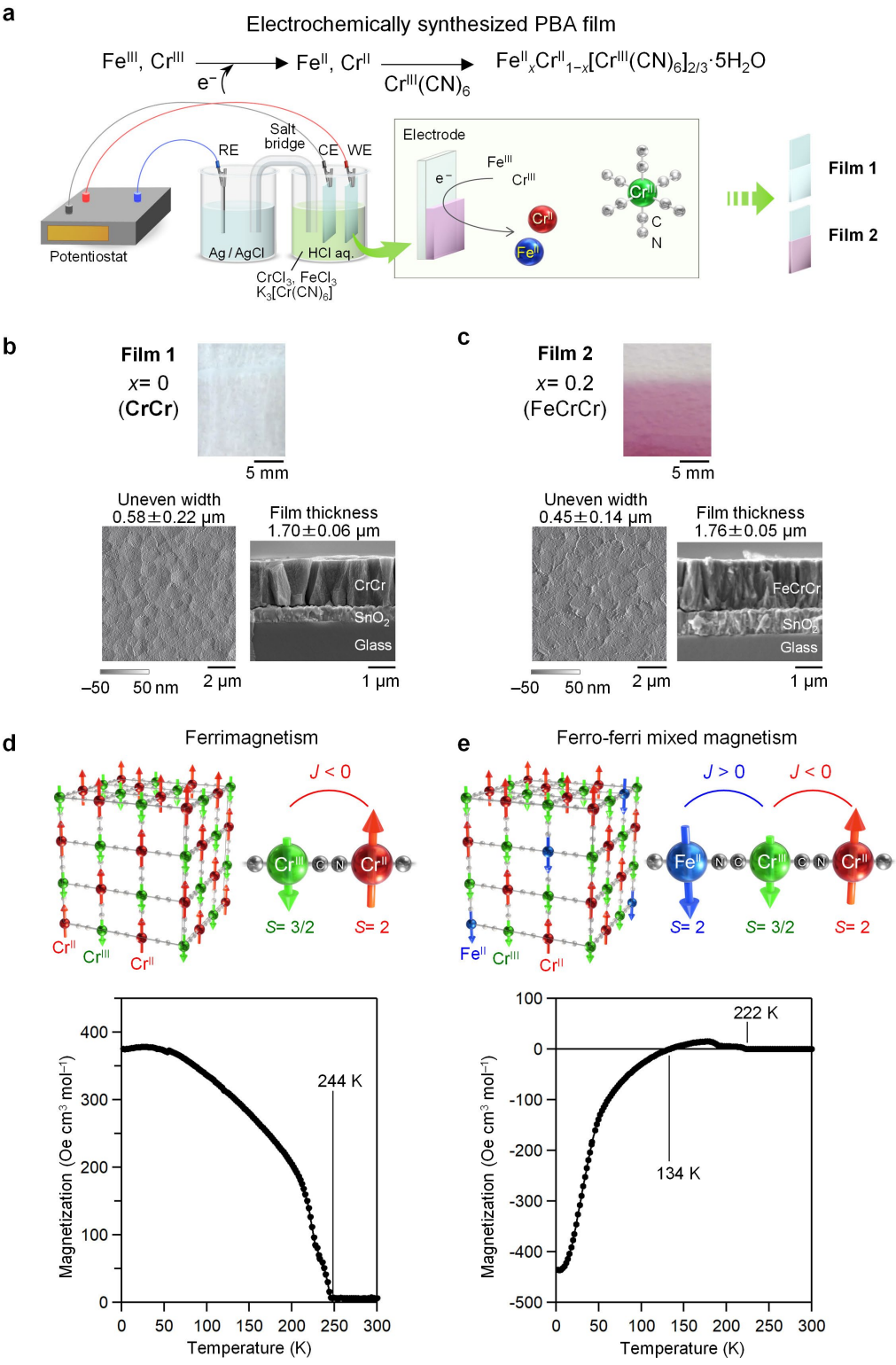

Figure 2. Electrochemically synthesized **Film 1** and **Film 2** (**a**). Photographs (upper), differential AFM images (lower left), and cross-sectional SEM images (lower right) of **Film 1** (**b**) and **Film 2** (**c**). The zero point of the AFM scale bar is set to the average position of surface irregularities. Magnetization vs. temperature plots of **Film 1** (**d**) and **Film 2** (**e**) under a 10 Oe out-of-plane magnetic field. The upper part of (**d**) is a schematic of the antiferromagnetic interactions between Cr^{II}(S= 2) and Cr^{III}(S= 3/2). The upper part of (**e**) is a schematic of mixed ferro-ferrimagnetism with ferromagnetic and antiferromagnetic interactions between Fe^{II}(S= 2) and Cr^{III}(S= 3/2) and between Cr^{II}(S= 2) and Cr^{III}(S= 3/2).

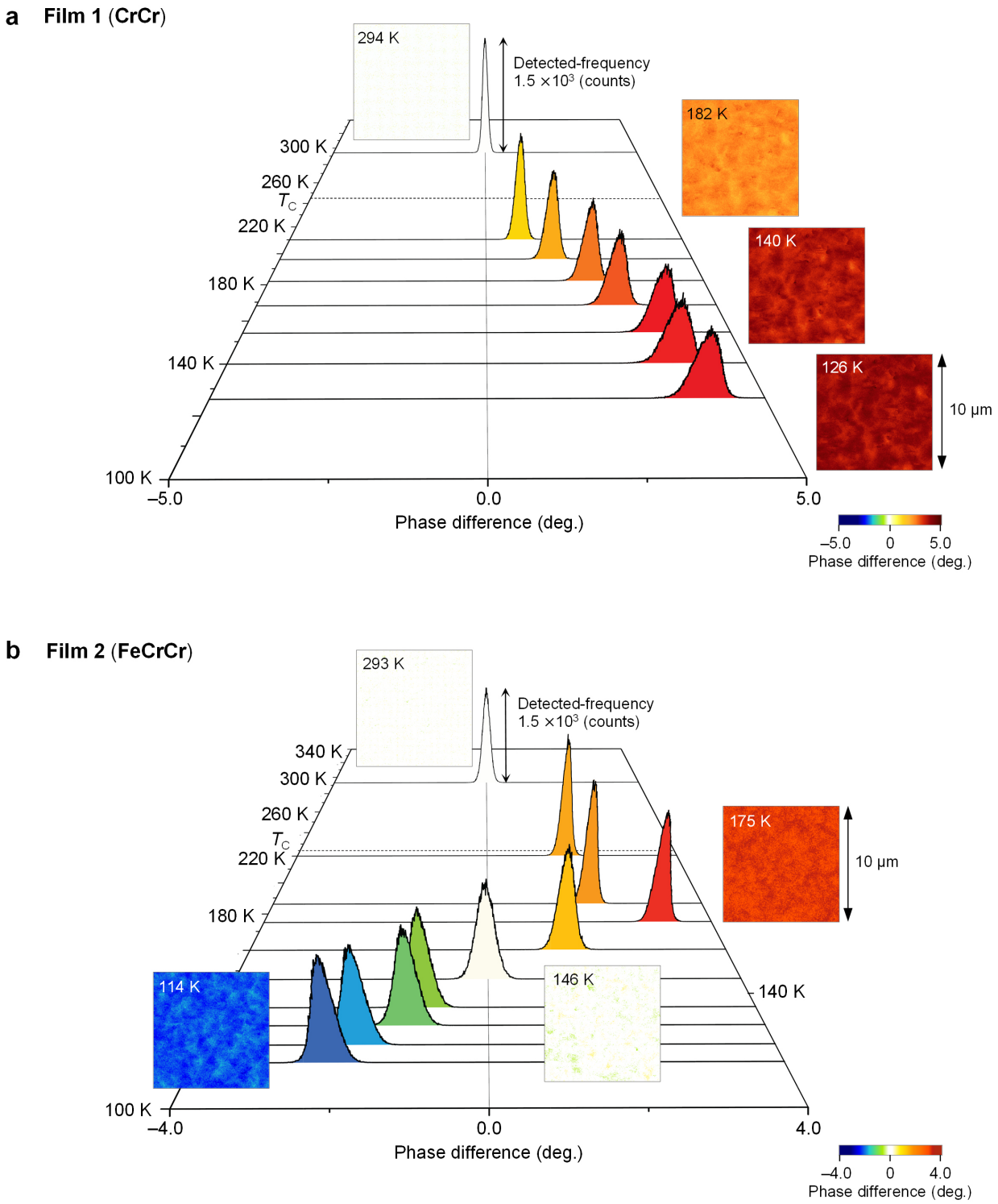

Figure 3. Temperature dependencies of the detected frequency vs. phase-difference determined from magnetic force microscopy (MFM) measurements of **Film 1** (**a**) and **Film 2** (**b**). The peak heights represent the detected frequencies. The insets are the MFM images measured at various temperatures.

1 at different temperatures, determined from the MFM measurements. Above T_C, at 294 K, the observed phase-difference was centered at zero, indicating the absence of a magnetic signal. After cooling to below T_C, **Film 1** showed a positive phase-difference indicating the development of positive magnetic polarization. Figure 4a shows the temperature dependence of the average phase-difference measured by MFM. This plot reproduces the magnetization curve of **Film 1** observed in magnetic measurements (Figure 2d). The MFM images in Figure 3a (inset) display the magnetic moment on the surface of **Film 1**, obtained by mapping the phase differences. As **Film 1** cooled, its magnetic polarization was enhanced, and its magnetic domains were clarified (Figures S13 and S14). The

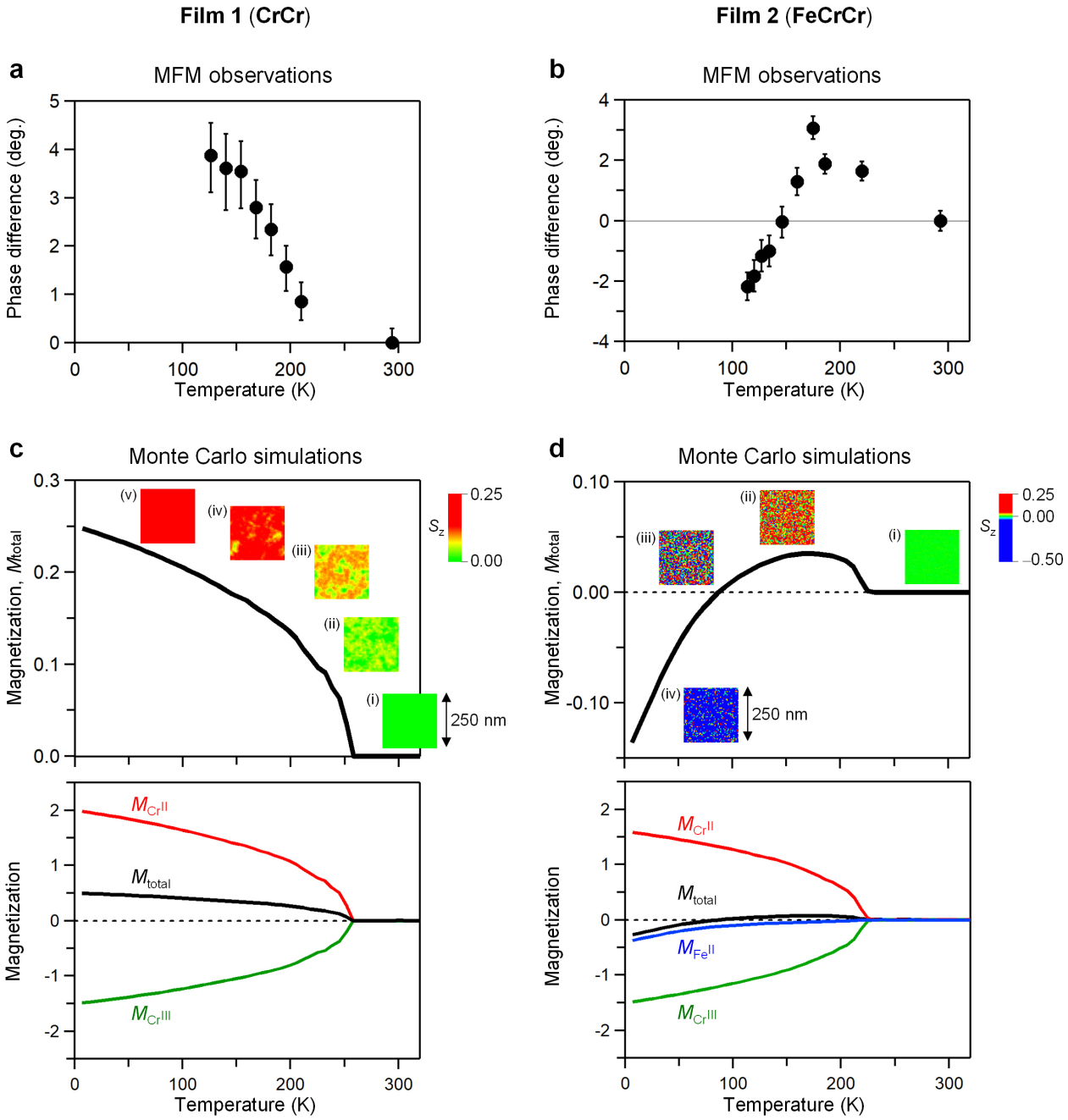

Figure 4. Observed temperature dependences of the phase-difference in MFM measurements of **CrCr** (**Film 1**) (**a**) and **FeCrCr** (**Film 2**) (**b**). Calculated total magnetization (M_{total}) vs. temperature curves under zero external magnetic field (upper) and calculated magnetizations vs. temperature curves in each sublattice (lower) of **CrCr** (**c**) and **FeCrCr** (**d**). The black, red, green, and blue lines plot the temperature dependences of M_{total}, $M_{Cr}{}^{II}$, $M_{Cr}{}^{III}$, and $M_{Fe}{}^{II}$, respectively. Insets are snapshots of the magnetization distributions. The color indicates the equilibrium magnetization (S_z) per-site, averaged over a block of 10 × 10 sites. Snapshots of **CrCr** at (i) 318 K, (ii) 252 K, (iii) 239 K, (iv) 205 K, and (v) 33 K, and **FeCrCr** at (i) 300 K, (ii) 159 K, (iii) 86 K ($M_{total} = 0$), and (iv) 13 K.

magnetic domains, represented by the color intensity, showed relatively strong and weak magnetic moments.

Figure 3b plots the detected frequency versus phase-difference on **Film 2** at different temperatures. As **Film 2** was cooled from 293 K to 175 K, the phase-difference peak shifted in the positive direction, but further cooling from 175 K to 114 K induced a negative shift. These shifts indicate that cooling from 293 K to 175 K generates positive magnetic polarization, but cooling from 175 K to 114 K generates negative magnetic polarization. Figure 4b plots the temperature dependence of the average phase-difference in **Film 2**. This plot reproduces the magnetic reversal behavior observed in the magnetic measurements (Figure 2e). The particular temperature T_p, at which the magnetic polarization vanishes, was around 146 K. The MFM images (Figure 3b, inset) visualize the magnetic moments on the surface of **Film 2**. No magnetic signal was detected at 293 K. Cooling induced a positive magnetic polarization and magnetic domains with relatively strong and weak magnetic moments were formed at 175 K (Figures S15

and S16). As the temperature further decreased, the positive magnetic polarization weakened and magnetic signal was scarcely detectable at T_p (146 K). Negative magnetic polarization weakly emerged at 134 K and was enhanced with further cooling. Based on these observations, magnetization reversal occurred as a gradual change from a positive magnetization state to a demagnetized state and finally to a negative magnetization state.

Mechanism of Compensation Temperature

To understand the temperature-induced magnetization reversal, Monte Carlo calculations of the Heisenberg spin model were implemented in a cubic lattice system composed of two sublattices (A and B) at the metal sites (Figure S17). The Heisenberg Hamiltonian is described as $H = -\sum_{<ij>} 2J_{ij} \vec{S}_i \cdot \vec{S}_j$, where $<ij>$ denotes nearest-neighbor coupling. In the **CrCr**-system (**Film 1**), the A and B sites were occupied by Cr^{III} (S = 3/2) and Cr^{II} (S = 2), respectively. In the **FeCrCr**-system (**Film 2**), Cr^{II} (S = 2) and Fe^{II} (S = 2) were randomly aligned at a ratio of 4:1. The Monte Carlo simulation was conducted in a system of 500 × 500 × 10 sites with periodic boundary conditions. The per-site magnetization was defined as $M_{total} = \left\langle \frac{1}{N} \sum_i S_i^z \right\rangle$, where $\langle \ \rangle$ denotes the thermal average and N is the number of all sites. Similarly, M_{Cr}^{III}, M_{Cr}^{II}, and M_{Fe}^{II} were defined for Cr^{III}, Cr^{II}, and Fe^{II} sites, respectively, where N is the number of sublattice sites. The model and calculation method are detailed in Supporting Information §16 (Figures S17 and S18). The upper and lower parts of Figure 4c show the calculated temperature dependencies of the total and sublattice magnetizations in the **CrCr**-system, respectively. The equivalent results of the **FeCrCr**-system are shown in Figure 4d. Both systems showed paramagnetic states above T_C but growing magnetization when cooled below T_C. In the **CrCr**-system, the sublattice magnetizations of Cr^{II} (M_{Cr}^{II}) and Cr^{III} (M_{Cr}^{III}) were positive and negative, respectively. The total magnetization (M_{total}) monotonously increased during cooling, indicating ferrimagnetic behavior. In the **FeCrCr**-system, M_{Cr}^{II} was positive but the M_{Cr}^{III} and sublattice magnetization of Fe^{II} (M_{Fe}^{II}) were negative. As this system was cooled below T_C, the total magnetization initially remained positive but eventually disappeared. Further cooling induced negative magnetization. The temperature dependence of magnetization in **FeCrCr** was interpreted as follows.: As Cr^{II} and Cr^{III} undergo stronger superexchange interactions than Fe^{II} and Cr^{III}, the growth of M_{Fe}^{II} is delayed relative to the growths of M_{Cr}^{II} and M_{Cr}^{III} (see lower part of Figure 4d), so the magnetization reverses. The insets of Figure 4c and 4d are snapshots of the magnetization distributions. Here, the color indicates the equilibrium magnetization per-site, averaged over blocks of 10 × 10 sites: red (positive magnetization), yellow (slightly positive magnetization), green (almost zero magnetization), light blue (slightly negative magnetization), and blue (negative magnetization). Each snapshot is an approximately 250 nm × 250 nm section of the actual sample. These snapshots re-confirm that magnetization reversal occurs via a gradual change from the positive magnetization state through demagnetization to a negative magnetization state.

Magnetic Domain

Next, we focused on the magnetic domain. Figure 5a shows the AFM and MFM images of **Film 1** at 154 K, the most stable temperature of the MFM equipment. Figure 5b combines the AFM and MFM images as three-dimensional topographic surface images with color maps of the magnetic moments. The magnetic domains (represented by color intensity) indicate both relatively strong and weak magnetic moments. The magnetic domains extended far beyond the primary crystalline size (ca. 60 nm) estimated by the Rietveld analysis and were larger than the uneven width (ca. 0.6 μm) estimated from the AFM observations (Figure S19). Figure 5c shows the MFM image simplified to two colors through image processing (see Method section). A maze pattern appears in the image. The magnetic domain size was estimated as one-to-several micrometers (approximately 0.67 ± 0.35 μm in width and 2.50 ± 0.72 μm in length, as estimated from Figures 5c and S20a), the typical size of single magnetic domains reported in conventional metal–alloy and metal–oxide magnets.[49–53] Figure 6 shows the AFM and MFM images of **Film 2** at 175, 146 and 114 K, respectively. At 175 K, positive magnetization was observed and the magnetic domain exhibited a maze pattern. **Film 2** at 175 K

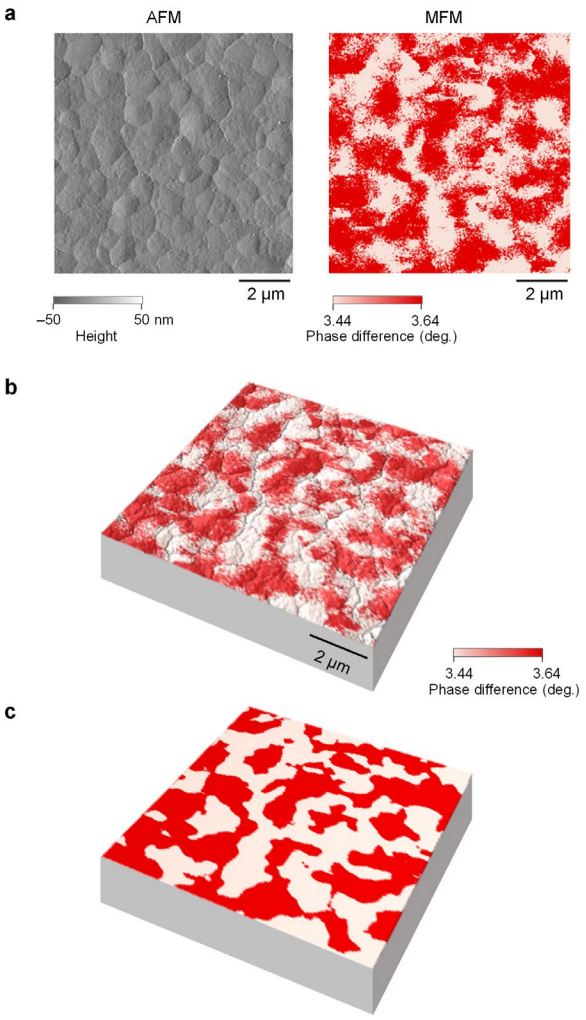

Figure 5. Atomic force microscopy (AFM) image (left) and MFM image (right) of **Film 1** at 154 K (**a**), 3D topographic AFM image with color mapping of the magnetization state of the surface, obtained from the MFM image (**b**). The zero point of the AFM scale bar is set to the average position of surface irregularities. Red and pale areas indicate where the magnetic moment is strong and weak, respectively. Bicolor mapping of the magnetization state obtained by image processing, showing a maze pattern (**c**).

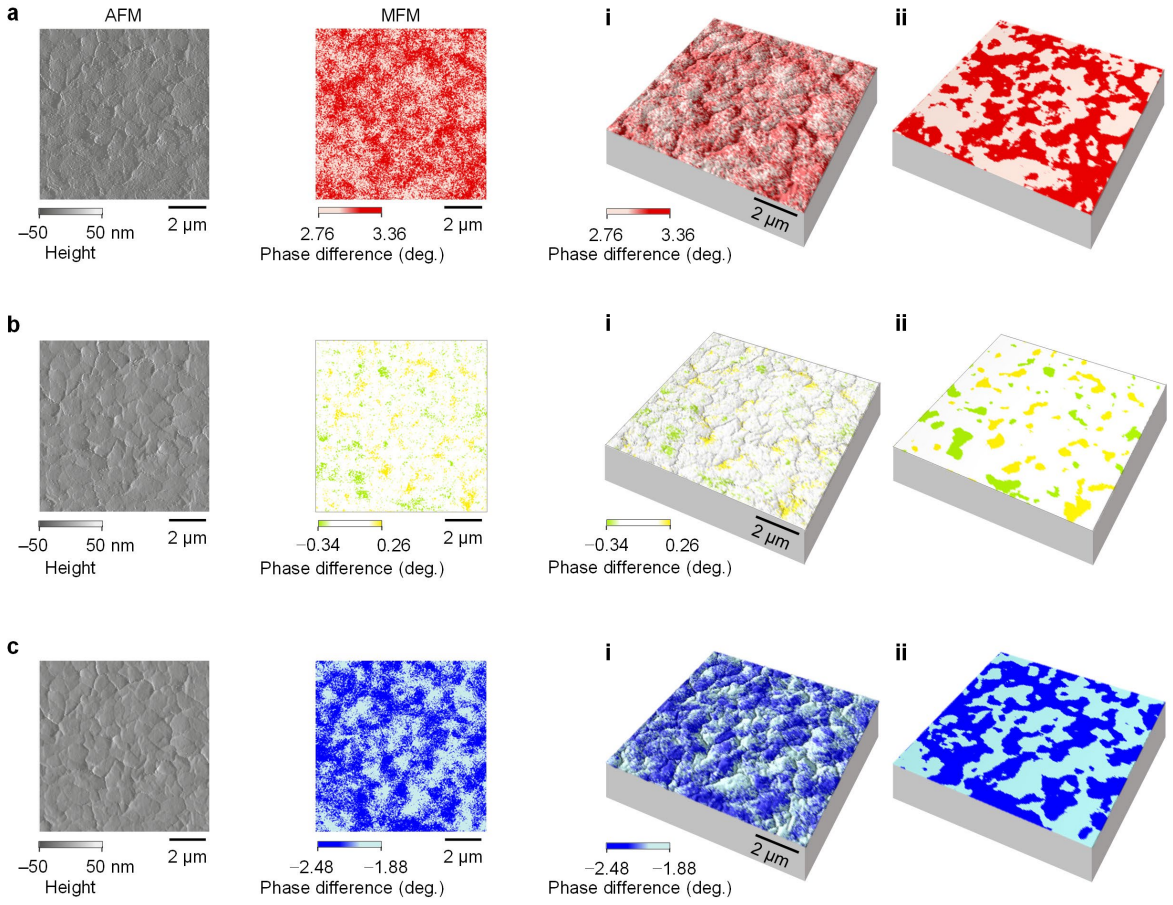

Figure 6. AFM (left) and MFM (middle) images of **Film 2** at 175 K (**a**), 146 K (**b**), and 114 K (**c**). The figures on the right are 3D topographic AFM images with color mapping of the magnetization state of the surface obtained from the MFM image (**i**) and bicolor mapping of the magnetization state obtained using image processing (**ii**).

displayed finer magnetic domains compared to **Film 1** at 154 K due to significant thermal fluctuations. At the compensation point (146 K), occasionally, regions with weak positive magnetization (yellow) and weak negative magnetization (green) were observed, but overall, the magnetization was nearly zero. At 114 K, negative magnetization was evident, and the magnetic domain pattern showed a maze pattern. As the temperature decreased, thermal fluctuations were relatively suppressed, resulting in the clear observation of magnetic domains compared to those observed at 175 K. The observed magnetic domain sizes in **Film 2** at 114 K were approximately 0.61 ± 0.27 μm in width and 2.12 ± 1.13 μm in length (Figure S20b), slightly smaller than the domain sizes of **Film 1** at 154 K. These differences suggest that thermal fluctuations had stronger influence on **Film 2** at 114 K compared to **Film 1** at 154 K.

Magnetic Domain under an External Magnetic Field

The left and right parts of Figure 7 show MFM images of **Film 1** under magnetic fields of +5 kOe and –5 kOe, respectively, applied parallel to the film surface (Figure 7a). The maze pattern of the magnetic domain in the absence of a magnetic field became a vertically striped pattern under the magnetic field (Figures 7b and S21). Figure 7c is a schematic of the relationship between the MFM signal and the magnetic moment (magnetic pole) on the film surface. The magnetic domain boundaries were located at the boundaries of the uneven film surface (Figure S22). Switching the direction of the applied magnetic field switched the direction of the magnetic moment on the film surface. Figure 8 shows the MFM images obtained at three different temperatures, 175, 146, and 114 K, when an external magnetic field was applied to **Film 2**. Even in **Film 2**, the magnetic domains exhibited a vertically striped pattern under the applied magnetic field. However, interestingly, differences in the pattern were observed depending on the temperature (Figure S21). At 175 K, the pattern was closer to a maze-like vertically-striped pattern. Upon cooling, the stripes became more distinct and transformed into a clear vertically striped pattern. This behavior can be interpreted as follows: at 175 K, strong thermal fluctuations hinder the ordering of the stripe pattern; however, as the temperature decreases, the thermal fluctuations are suppressed, leading to a more distinct vertically striped pattern.

CONCLUSIONS

To observe the magnetic domains of molecule-based magnets, we focused on the electrochemically synthesized films of two Prussian blue analogs: **CrCr** (**Film 1**, $Cr[Cr(CN)_6]_{2/3}{\cdot}5H_2O$) and **FeCrCr** (**Film 2**, $Fe_{0.20}Cr_{0.80}[Cr(CN)_6]_{2/3}{\cdot}5.3H_2O$). Magnetic polarization was generated and grown in **Film 1**. The magnetic domains of this film showed a maze pattern with a domain size of one-to-several micrometers, a reasonable size for single magnetic domains. Under a magnetic field, the shape of the magnetic domain changed from a maze to a vertically-

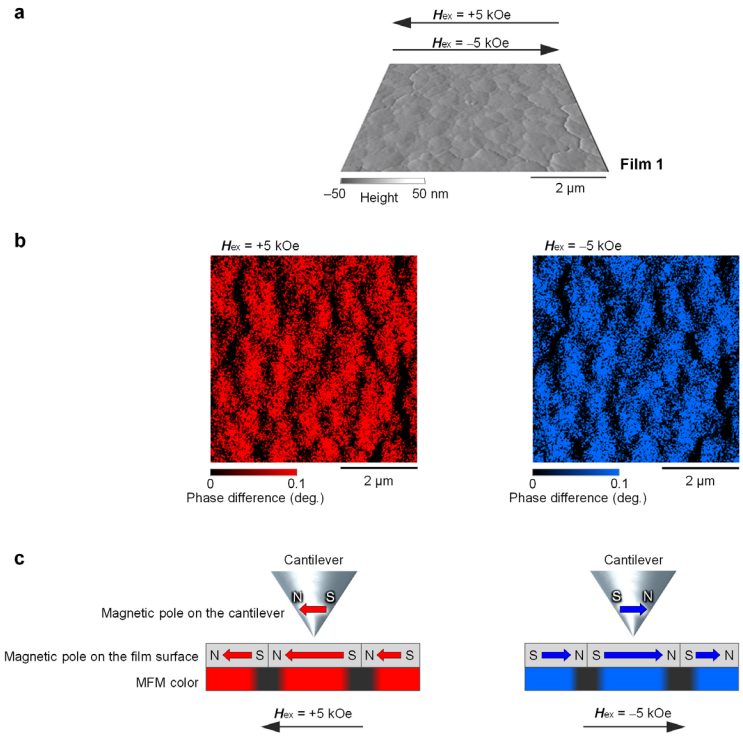

Figure 7. Configurations of the external magnetic fields (H_{ex}= ±5 kOe) applied to the film (**a**), MFM images measured at 153 K under H_{ex} = +5 kOe (left) and −5 kOe (right) (**b**), and schematic representation of the relationships between the magnetic moment (magnetic pole) on the film surface and cantilever (**c**).

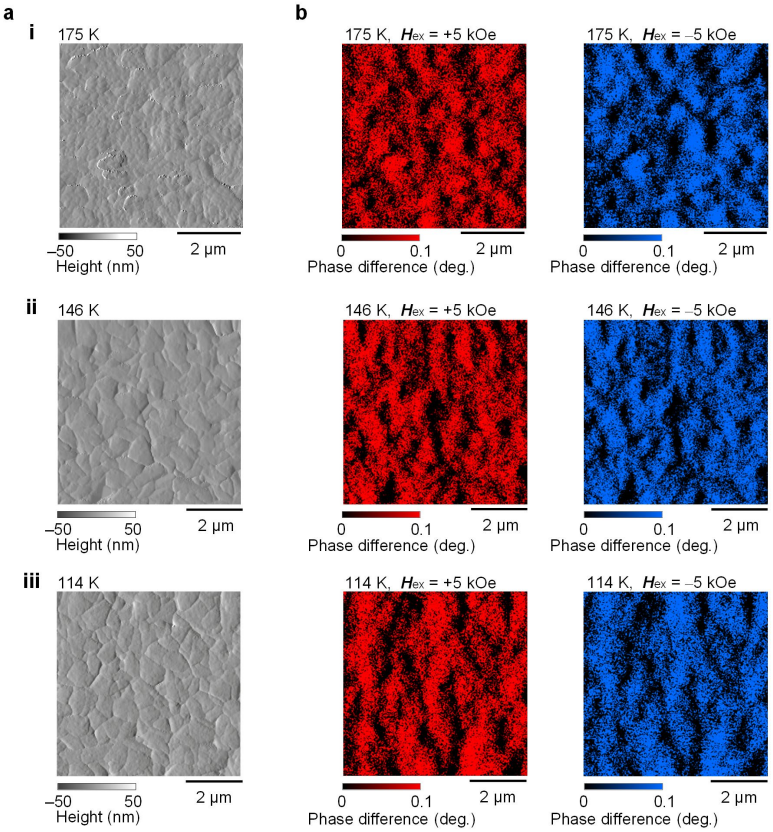

Figure 8. AFM (**a**) and MFM (**b**) images of **Film 2** measured at 175 K (**i**), 146 K (**ii**), and 114 K (**iii**) under H_{ex} = +5 kOe (middle) and −5 kOe (right). The observed regions vary at each temperature.

striped pattern. Meanwhile, **Film 2** exhibited magnetization reversal behavior in the MFM measurements. The observations showed that magnetization reversal was achieved through a gradual change from positive magnetization to demagnetization and finally to negative magnetization. Such a temperature evolution of surface-magnetization at the magnetization reversal has not been previously reported. This process differs from that of induced magnetization reversal under an external magnetic field, which reverses the magnetic-domain sizes of positive and negative magnetic moment. Temperature-induced magnetization reversal via positive magnetization through demagnetization to negative magnetization was further confirmed in Monte Carlo simulations.

Energy-conservative recording media are urgently demanded in modern society.[54–58] From this viewpoint, research related to magnetization reversal is an important issue. The observation of temperature-induced magnetization reversal is of great importance for the basic understanding and engineering of magnetic materials. Furthermore, this work shows that the field of molecule-based magnets is possible to expand from magnetochemistry to magnetostatic engineering of bulk magnets, and open a new field of molecule-based magnetostatic engineering.

EXPERIMENTAL SECTION

Materials

Elemental analyses of the prepared samples yielded a formula of $Cr^{II}[Cr^{III}(CN)_6]_{2/3}\cdot 5H_2O$ (**CrCr**) for **Film 1** (Calcd: Cr, 30.86; C, 17.11; N, 19.96 wt%. Found: Cr, 30.59; C, 17.31; N, 19.83 wt%) and $Fe_{0.20}Cr_{0.80}[Cr(CN)_6]_{2/3}\cdot 5.3H_2O$ (**FeCrCr**) for **Film 2** (Calcd: Fe, 3.89; Cr, 26.57; C, 16.74; N, 19.52 wt%. Found: Fe, 3.66; Cr, 26.93; C, 16.81; N, 19.22 wt%).

Physical measurements

Elemental analyses for Fe and Cr were performed using an Agilent 7700x inductively coupled plasma mass spectroscopy, while those for C and N were performed using standard microanalytical methods. X-ray diffraction (XRD) measurements were performed using a Rigaku Ultima IV diffractometer with Cu Kα radiation (λ = 1.5418 Å). The PDXL program (Rigaku) was used for the Rietveld analyses. UV–vis absorption spectra were measured on a JASCO V-770 spectrometer. Infrared (IR) spectra were recorded on a JASCO FT/IR-4700 spectrometer. The microstructures of the film samples were measured using a SEM (JEOL JSM-7800F PRIME) with a JEOL JED-2300F accessory for Energy Dispersive X-ray Spectroscopy (EDS) and with a field-emission transmission electron microscopy (TEM) (EF-TEM, JEOL JEM-2800F) in conjunction with EDS using an X-MAX 100TLE SDD detector (Oxford Instruments). The magnetic properties were measured using a SQUID magnetometer (Quantum Design, MPMS 7).

Principles of MFM measurement

MFM is a magnetization detection technique that sensitively responds to the magnetization of a sample surface. In MFM measurement, a magnetic moment is detected by scanning a sample surface with a magnetic probe (cantilever). The magnetic moment is detected as a phase difference between the cantilever oscillations (Supporting Information §11). The strength of the magnetic moment is detected as magnitude of the phase difference, while the direction of the magnetic moment (positive or negative) is detected as the direction of the phase difference between the oscillations of the cantilever.

AFM and MFM measurements

AFM and MFM measurements were conducted using a Hitachi High-Tech Science AFM5000II/AFM5300E MFM with an SI-MF40 cantilever (Supporting Information §21 and Figure S23). To enable MFM measurements at different temperatures, an optional heating–cooling dual-purpose sample stage, a cooling Dewar, and a temperature controller were attached to the AFM5000II/AFM5300E. For external magnetic field application, a custom-made setup was implemented, which involved placing an electromagnet beside the sample stage and controlling the current flowing through the electromagnet to achieve magnetic field control ranging from −5 kOe to +5 kOe. A magnetic field was applied horizontally to the thin film sample mounted on the sample stage.

Stray field from the magnetic cantilever and initial magnetization condition

The magnetic cantilever used in the MFM measurement, SI-MF40, is a silicon cantilever coated with an 80-nm-thick CoPtCr magnetic film. The setting parameter of Z_{lift} was set to 50 nm. The stray field of the cantilever operates in an extremely narrow region of several tens of nanometers and is estimated to have a strength of approximately 400 Oe (Supporting Information §21). The stray field generated by the magnetic cantilever is a localized dynamic magnetic field, and its effect is different from that of applying a static magnetic field over a wide area, suggesting that it may not considerably change the pattern of microscale magnetic domains. Regarding the initial magnetization conditions in this MFM measurement, an external magnetic field was not applied to set the initial magnetization direction, i.e., the stray magnetic field from the magnetic probe was solely relied.

Estimation of uneven widths from AFM images

The uneven widths of the film sample surfaces were estimated by analyzing AFM images as follows: we selected 100 clearly visible uneven widths for each AFM image and measured their diameters using the “Image J” software. This process was repeated for six AFM images, resulting in 600 uneven width measurements. Subsequently, we derived the distribution of uneven widths and calculated the average values (Figure S2).

Estimation of the magnetic domain size from MFM images

The sizes of the magnetic domains were estimated as follows: in the bicolor-mapped MFM images, we measured the values of 126 short and 37 long widths of magnetic domains using the “Image J” software (Figure S20). Subsequently, we calculated the distribution and average values for both the short and long widths.

Image processing

As a first step, the effect “Blur (Gaussian)” was applied to the target image using Adobe’s After Effects software. This treatment was performed by weighting the values of the surrounding pixels for a given pixel by a Gaussian function according to their distance and superimposing them. The used parameter is 95. As a second step, the After Effects “Tone Curve” was applied to the above-processed image, thresholded, and binarized.

ASSOCIATED CONTENT

Supporting Information. Supplementary AFM images, IR and UV-vis spectra, XRD patterns, magnetization vs. field curves, MFM measurement details, supplementary MFM images, temperature-dependent phase distributions, and Monte Carlo simulation details. This material is available free of charge via the internet at http://pubs.acs.org.

AUTHOR INFORMATION

Corresponding Author

*ohkoshi@chem.s.u-tokyo.ac.jp; tokoro@ims.tsukuba.ac.jp

Author Contributions

The manuscript was written through contributions of all authors. All authors have given approval to the final version of the manuscript.

ACKNOWLEDGMENT

The present research was supported in part by a JSPS Grant-in-Aid for Scientific Research (B) (22H02046), Scientific Research (A) (20H00369), Tsukuba Basic Research Support Program (Type S), and the JST SPRING program (JPMJSP2124). We acknowledge the Cryogenic Research Center, The University of Tokyo, the Center for Nano Lithography & Analysis, The University of Tokyo supported by MEXT, and the Quantum Leap Flagship Program (Q-LEAP) supported by MEXT. We are grateful to Prof. Asuka Namai for her technical support, Mr. S. Ohtsuka and Mr. M. Fukukawa for collecting the SEM images, and Mr. H. Oshikawa for collecting the TEM images.

REFERENCES

(1) Kahn, O. Blueprint for success. *Nature* **1995**, *378*, 667–668.

(2) Perlepe, P.; Oyarzabal, I.; Voigt, L.; Kubus, M.; Woodruff, D. N.; Reyes-Lillo, S. E.; Aubrey, M. L.; Négrier, P.; Rouzières, M.; Wilhelm, F.; Rogalev, A.; Neaton, J. B.; Long, J. R.; Mathonière, C.; Vignolle, B.; Pedersen, K. S.; Clérac, R. From an antiferromagnetic insulator to a strongly correlated metal in square-lattice $MCl_2(pyrazine)_2$ coordination solid. *Nat. Commun.* **2022**, *13*, 5766.

(3) Park, J. G.; Collins, B. A.; Darago, L. E.; Runčevski, T.; Ziebel, M. E.; Aubrey, M. L.; Jiang, H. Z. H.; Velasquez, E.; Green, M. A.; Goodpaster, J. D.; Long, J. R. Magnetic ordering through itinerant ferromagnetism in a metal–organic framework. *Nat. Chem.* **2021**, *13*, 594–598.

(4) Oh, I.; Park, J.; Choe, D.; Jo, J.; Jeong, H.; Jin, M. J.; Jo, Y.; Suh, J.; Min, B. C.; Yoo, J. W. A scalable molecule-based magnetic thin film for spin-thermoelectric energy conversion. *Nat. Commun.* **2021**, *12*, 1057.

(5) Zhang, J.; Kosaka, W.; Kitagawa, Y.; Miyasaka, H. A metal–organic framework that exhibits CO_2-induced transitions between paramagnetism and ferrimagnetism. *Nat. Chem.* **2021**, *13*, 191–199.

(6) Perlepe, P.; Oyarzabal, I.; Mailman, A.; Yquel, M.; Platunov, M.; Dovgaliuk, I.; Rouzières, M.; Négrier, P.; Mondieig, D.; Suturina, E. A.; Dourges, M. A.; Bonhommeau, S.; Musgrave, R. A.; Pedersen, K. S.; Chernyshov, D.; Wilhelm, F.; Rogalev, A.; Mathonière, C.; Clérac, R. Metal-organic magnets with large coercivity and ordering temperatures up to 242°C. *Science* **2020**, *370* (6516), 587–592.

(7) Coronado, E. Molecular magnetism: from chemical design to spin control in molecules, materials and devices. *Nat. Rev. Mater.* **2020**, *5*, 87–104.

(8) Ohkoshi, S.; Takano, S.; Imoto, K.; Yoshikiyo, M.; Namai, A.; Tokoro, H. 90-degree optical switching of output second harmonic light in chiral photomagnet. *Nat. Photon.* **2014**, *8*, 65–71.

(9) Heintze, E.; Hallak, F. E.; Clauß, C.; Rettori, A.; Pini, M. G.; Totti, F.; Dressel, M.; Bogani, L. Dynamic control of magnetic nanowires by light-induced domain-wall kickoffs. *Nat. Mater.* **2013**, *12*, 202–206.

(10) Train, C.; Gheorghe, R.; Krstic, V.; Chamoreau, L. M.; Ovanesyan, N. S.; Rikken, G. L. J. A.; Gruselle, M.; Verdaguer, M. Strong magneto-chiral dichroism in enantiopure chiral ferromagnets. *Nat. Mater.* **2008**, *7*, 729–734.

(11) Miller, J. S.; Manson, J. L. Designer Magnets Containing Cyanides and Nitriles. *Acc. Chem. Res.* **2001**, *34* (7), 563–570.

(12) Coronado, E.; Galán-Mascarós, J. R.; Gomez-Garcia, C. J.; Laukhin, V. Coexistence of ferromagnetism and metallic conductivity in a molecule-based layered compound. *Nature* **2000**, *408*, 447–449.

(13) Hatlevik, Ø.; Buschmann, W. E.; Zhang, J.; Manson, J. L.; Miller, J. S. Enhancement of the Magnetic Ordering Temperature and Air Stability of a Mixed Valent Vanadium Hexacyanochromate(III) Magnet to 99 °C (372 K) *Adv. Mater.* **1999**, *11* (11), 914–918.

(14) Sato, O.; Iyoda, T.; Fujishima, A.; Hashimoto, K. Electrochemically tunable magnetic phase transition in a high-T_C chromium cyanide thin film. *Science* **1996**, *271*, 49–51.

(15) Ferlay, S.; Mallah, T.; Ouahès, R.; Veillet, P.; Verdaguer, M. A room-temperature organometallic magnet based on Prussian blue. *Nature* **1995**, *378*, 701–703.

(16) Entley, W. R.; Girolami, G. S. High-Temperature Molecular Magnets Based on Cyanovanadate Building Blocks: Spontaneous Magnetization at 230 K. *Science* **1995**, *268* (5209), 397–400.

(17) Mallah, T.; Thiébaut, S.; Verdaguer, M.; Veillet, P. High-T_C Molecular-Based Magnets: Ferrimagnetic Mixed-Valence Chromium(III)-Chromium(II) Cyanides with T_C at 240 and 190 Kelvin. *Science* **1993**, *262* (5139), 1554–1557.

(18) Tamaki, H.; Zhong, Z. J.; Matsumoto, N.; Kida, S.; Koikawa, M.; Achiwa, N.; Hashimoto, Y.; Okawa, H. Design of metal-complex magnets. Syntheses and magnetic properties of mixed-metal assemblies $\{NBu_4[MCr(ox)_3]\}_x$ (NBu_4^+ = Tetra(n-butyl)ammonium ion; ox^{2-} = Oxalate ion; M = Mn^{2+}, Fe^{2+}, Co^{2+}, Ni^{2+}, Cu^{2+}, Zn^{2+}). *J. Am. Chem. Soc.* **1992**, *114* (18), 6974–6979.

(19) Kinoshita, M.; Turek, P.; Tamura, M.; Nozawa, K.; Shiomi, D.; Nakazawa, Y.; Ishikawa, M.; Takahashi, M.; Awaga, K.; Inabe, T.; Maruyama, Y. An Organic Radical Ferromagnet. *Chem. Lett.* **1991**, *20* (7), 1225–1228.

(20) Manriquez, J. M.; Yee, G. T.; McLean, R. S.; Epstein, A. J.; Miller, J. S. A Room-Temperature Molecular/Organic-Based Magnet. *Science* **1991**, *252* (5011), 1415–1417.

(21) Kahn, O. The magnetic turnabout. *Nature* **1999**, *399*, 21–22.

(22) Verdaguer, M.; Bleuzen, A.; Marvaud, V.; Vaissermann, J.; Seuleiman, M.; Desplanches, C.; Scuiller, A.; Train, C.; Garde, R.; Gelly, G.; Lomenech, C.; Rosenman, I.; Veillet, P.; Cartier, C.; Villain, F. Molecules to build solids: high T_C molecule-based magnets by design and recent revival of cyano complexes chemistry. *Coord. Chem. Rev.* **1999**, *190–192*, 1023–1047.

(23) Ohkoshi, S.; Abe, Y.; Fujishima, A.; Hashimoto, K. Design and Preparation of a Novel Magnet Exhibiting Two Compensation Temperatures Based on Molecular Field Theory. *Phys. Rev. Lett.* **1999**, *82* (6), 1285–1288.

(24) Ohkoshi, S.; Hashimoto, K. Design of a Novel Magnet Exhibiting Photoinduced Magnetic Pole Inversion Based on Molecular Field Theory. *J. Am. Chem. Soc.* **1999**, *121* (45), 10591–10597.

(25) Hu, Y.; Broderick, S.; Guo, Z.; N'Diaye, A. T.; Bola, J. S.; Malissa, H.; Li, C.; Zhang, Q.; Huang, Y.; Jia, Q.; Boehme, C.; Vardeny, Z. V.; Zhou, C.; Ren, S. Proton switching molecular magnetoelectricity. *Nat. Commun.* **2021**, *12*, 4602.

(26) Cammarata, M.; Zerdane, S.; Balducci, L.; Azzolina, G.; Mazerat, S.; Exertier, C.; Trabuco, M.; Levantino, M.; Alonso-Mori, R.; Glownia, J. M.; Song, S.; Catala, L.; Mallah, T.; Matar, S. F.; Collet, E. Charge transfer driven by ultrafast spin transition in a CoFe Prussian blue analogue. *Nat. Chem.* **2021**, *13*, 10–14.

(27) Cain, J. M.; Felts, A. C.; Meisel, M. W.; Talham, D. R. Crafting Spin-State Switchable Strain Profiles within $Rb_xCo[Fe(CN)_6]_y@K_jNi[Cr(CN)_6]_k$ Heterostructures. *Chem. Matter.* **2021**, *33* (1), 246–255.

(28) Ohkoshi, S.; Nakagawa, K.; Imoto, K.; Tokoro, H.; Shibata, Y.; Okamoto, K.; Miyamoto, Y.; Komine, M.; Yoshikiyo, M.; Namai, A. A photoswitchable polar crystal that exhibits superionic conduction. *Nat. Chem.* **2020**, *12*, 338–344.

(29) Simonov, A.; Baerdemaeker, T. D.; Boström, H. L. B.; Gómez, M. L. R.; Gray, H. J.; Chernyshov, D.; Bosak, A.; Bürgi, H.-B.; Goodwin, A. L. Hidden diversity of vacancy networks in Prussian blue analogues. *Nature* **2020**, *578*, 256–260.

(30) Magott, M.; Reczyński, M.; Gaweł, B.; Sieklucka, B.; Pinkowicz, D. A Photomagnetic Sponge: High-Temperature Light-Induced Ferrimagnet Controlled by Water Sorption. *J. Am. Chem. Soc.* **2018**, *140* (46), 15876–15882.

(31) Espallargas, G. M.; Coronado, E. Magnetic functionalities in MOFs: from the framework to the pore. *Chem. Soc. Rev.* **2018**, *47* (2), 533–557.

(32) Felts, A. C.; Slimani, A.; Cain, J. M.; Andrus, M. J.; Ahir, A. R.; Abboud, K. A.; Meisel, M. W.; Boukheddaden, K.; Talham, D. R. Control of the Speed of a Light-Induced Spin Transition through Mesoscale Core–Shell Architecture. *J. Am. Chem. Soc.* **2018**, *140* (17), 5814–5824.

(33) Pinilla-Cienfuegos, E.; Mañas-Valero, S.; Forment-Aliaga, A.; Coronado, E. Switching the Magnetic Vortex Core in a Single Nanoparticle. *ACS Nano* **2016**, *10* (2), 1764–1770.

(34) Pinkowicz, D.; Rams, M.; Mišek, M.; Kamenev, K. V.; Tomkowiak, H.; Katrusiak, A.; Sieklucka, B. Enforcing Multifunctionality: A Pressure-Induced Spin-Crossover Photomagnet. *J. Am. Chem. Soc.* **2015**, *137* (27), 8795–8802.

(35) Gil-Hernández, B.; Savvin, S.; Makhloufi, G.; Núñez, P.; Janiak, C.; Sanchiz, J. Proton Conduction and Long-Range Ferrimagnetic Ordering in Two Isostructural Copper(II) Mesoxalate Metal–Organic Frameworks. *Inorg. Chem.* **2015**, *54* (4), 1597–1605.

(36) Pinilla-Cienfuegos, E.; Kumar, S.; Mañas-Valero, S.; Canet-Ferrer, J.; Catala, L.; Mallah, T.; Forment-Aliaga, A.; Coronado, E. Imaging the Magnetic Reversal of Isolated and Organized Molecular-Based Nanoparticles using Magnetic Force Microscopy. *Part. Part. Syst. Charact.* **2015**, *32* (6), 693–700.

(37) Risset, O. N.; Quintero, P. A.; Brinzari, T. V.; Andrus, M. J.; Lufaso, M. W.; Meisel, M. W.; Talham, D. R. Light-Induced Changes in Magnetism in a Coordination Polymer Heterostructure, $Rb_{0.24}Co[Fe(CN)_6]_{0.74}@K_{0.10}Co[Cr(CN)_6]_{0.70}\cdot nH_2O$ and the Role of the Shell Thickness on the Properties of Both Core and Shell. *J. Am. Chem. Soc.* **2014**, *136* (44), 15660–15669.

(38) Brossard, S.; Volatron, F.; Lisnard, L.; Arrio, M. A.; Catala, L.; Mathonière, C.; Mallah, T.; Cartier dit Moulin, C.; Rogalev, A.; Wilhelm, F.; Smekhova, A.; Sainctavit, P. Investigation of the Photoinduced Magnetization of Copper Octacyanomolybdates Nanoparticles by X-ray Magnetic Circular Dichroism. *J. Am. Chem. Soc.* **2012**, *134* (1), 222–228.

(39) Pardo, E.; Train, C.; Gontard, G.; Boubekeur, K.; Fabelo, O.; Liu, H.; Dkhil, B.; Lloret, F.; Nakagawa, K.; Tokoro, H.; Ohkoshi, S.; Verdaguer, M. High Proton Conduction in a Chiral Ferromagnetic Metal-Organic Quartz-like Framework. *J. Am. Chem. Soc.* **2011**, *133* (39), 15328–15331.

(40) Ohkoshi, S.; Imoto, K.; Tsunobuchi, Y.; Takano, S.; Tokoro, H. Light-induced spin-crossover magnet. *Nat. Chem.* **2011**, *3*, 564–569.

(41) Avendano, C.; Hilfiger, M. G.; Prosvirin, A.; Sanders, C.; Stepien, D.; Dunbar, K. R. Temperature and Light Induced Bistability in a $Co_3[Os(CN)_6]_2$ $6H_2O$ Prussian Blue Analog. *J. Am. Chem. Soc.* **2010**, *132* (38), 13123–13125.

(42) Tokoro, H.; Matsuda, T.; Nuida, T.; Moritomo, Y.; Ohoyama, K.; Dangui, E. D. L.; Boukheddaden, K.; Ohkoshi, S. Visible-Light-Induced Reversible Photomagnetism in Rubidium Manganese Hexacyanoferrate. *Chem. Mater.* **2008**, *20* (2), 423–428.

(43) Coronado, E.; Giménez-López, M. C.; Levchenko, G.; Romero, F. M.; García-Baonza, V.; Milner, A.; Paz-Pasternak, M. Pressure-Tuning of Magnetism and Linkage Isomerism in Iron(II) Hexacyanochromate. *J. Am. Chem. Soc.* **2005**, *127* (13), 4580–4581.

(44) Kaye, S. S.; Long, J. R. Hydrogen Storage in the Dehydrated Prussian Blue Analogues $M_3[Co(CN)_6]_2$ (M = Mn, Fe, Co, Ni, Cu, Zn). *J. Am. Chem. Soc.* **2005**, *127* (18), 6506–6507.

(45) Ohkoshi, S.; Arai, K.; Sato, Y.; Hashimoto, K. Humidity-induced magnetization and magnetic pole inversion in a cyano-bridged metal assembly. *Nat. Mater.* **2004**, *3*, 857–861.

(46) Herrera, J. M.; Marvaud, V.; Verdaguer, M.; Marrot, J.; Kalisz, M.; Mathonière, C. Reversible Photoinduced Magnetic Properties in the Heptanuclear Complex $[Mo^{IV}(CN)_2(CN–CuL)_6]^{8+}$: A Photomagnetic High-Spin Molecule. *Angew. Chem. Int. Ed.* **2004**, *43* (41), 5468–5471.

(47) Renz, F.; Oshio, H.; Ksenofontov, V.; Waldeck, M.; Spiering, H.; Gütlich, P. Strong Field Iron(II) Complex Converted by Light into a Long-Lived High-Spin State. *Angew. Chem. Int. Ed.* **2000**, *39* (20), 3699–3700.

(48) Ohkoshi, S.; Fujishima, A.; Hashimoto, K. Transparent and Colored Magnetic Thin Films: $(Fe^{II}_xCr^{II}_{1-x})_{1.5}[Cr^{III}(CN)_6]$. *J. Am. Chem. Soc.* **1998**, *120* (21), 5349–5350.

(49) Luo, Z.; Hrabec, A.; Dao, T. P.; Sala, G.; Finizio, S.; Feng, J.; Mayr, S.; Raabe, J.; Gambardella, P.; Heyderman, L. J. Current-driven magnetic domain-wall logic. *Nature* **2020**, *579*, 214–218.

(50) Szmaja, W. Investigations of the domain structure of anisotropic sintered Nd–Fe–B-based permanent magnets. *J. Magn. Magn. Mater.* **2006**, *301* (2), 546–561.

(51) Portmann, O.; Vaterlaus, A.; Pescia, D. An inverse transition of magnetic domain patterns in ultrathin films. *Nature* **2003**, *422*, 701–704.

(52) Castrucci, P.; Gunnella, R.; Bernardini, R.; Falcioni, P.; Crescenzi, M. D. Magnetic force microscopy study of perpendicular magnetization reorientation for Fe grown on Cu/Si(111). *Phys. Rev. B* **2002**, 65, 235435.

(53) Yang, J.; Mao, W.; Cheng, B.; Yang, Y. Magnetic properties and magnetic domain structures of $NdFe_{10.5}Mo_{1.5}$ and $NdFe_{10.5}Mo_{1.5}N_x$. *Appl. Phys. Lett.* **1997**, *71* (22), 3290–3292.

(54) Zhang, Y.; Fowler, C.; Liang, J.; Azhar, B.; Shalaginov, M. Y.; Deckoff-Jones, S.; An, S.; Chou, J. B.; Roberts, C. M.; Liberman, V.; Kang, M.; Ríos, C.; Richardson, K. A.; Rivero-Baleine, C.; Gu, T.; Zhang, H.; Hu, J. Electrically reconfigurable non-volatile metasurface using low-loss optical phase-change material. *Nat. Nanotech.* **2021**, *16*, 661–666.

(55) Ohkoshi, S.; Yoshikiyo, M.; Imoto, K.; Nakagawa, K.; Namai, A.; Tokoro, H.; Yahagi, Y.; Takeuchi, K.; Jia, F.; Miyashita, S.; Nakajima, M.; Qiu, H.; Kato, K.; Yamaoka, T.; Shirata, M.; Naoi, K.; Yagishita, K.; Doshita, H. Magnetic-Pole Flip by Millimeter Wave. *Adv. Mater.* **2020**, *32* (48), 2004897.

(56) Caretta, L.; Mann, M.; Büttner, F.; Ueda, K.; Pfau, B.; Günther, C. M.; Hessing, P.; Churikova, A.; Klose, C.; Schneider, M.; Engel, D.; Marcus, C.; Bono, D.; Bagschik, K.; Eisebitt, S.; Beach, G. S. D. Fast current-driven domain walls and small skyrmions in a compensated ferrimagnet. *Nat. Nanotech.* **2018**, *13*, 1154–1160.

(57) Stupakiewicz, A.; Szerenos, K.; Afanasiev, D.; Kirilyuk, A.; Kimel, A. V. Ultrafast nonthermal photo-magnetic recording in a transparent medium. *Nature* **2017**, *542*, 71–74.

(58) Avci, C. O.; Quindeau, A.; Pai, C. F.; Mann, M.; Caretta, L.; Tang, A. S.; Onbasli, M. C.; Ross, C. A.; Beach, G. S. D. Current-induced switching in a magnetic insulator. *Nat. Mater.* **2017**, *16*, 309–314.

SYNOPSIS TOC

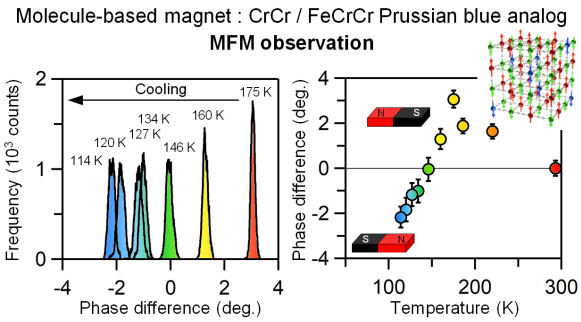

The magnetic domains in molecule-based magnets of two Prussian blue analogs, $Fe_xCr_{1-x}[Cr(CN)_6]_{2/3}$ films (x= 0; **Film 1** and x= 0.2; **Film 2**), were studied using magnetic force microscopy (MFM). **Film 1** shows magnetic domain below T_C with a maze pattern. In **Film 2**, positive magnetic polarization appears below T_C and magnetization becomes zero at a particular temperature, changing the magnetic polarization to negative.